Measurement report: size-resolved particle effective density measured by the AAC-SMPS and implications for chemical composition

Yao Song[1], Jing Wei[1], Wenlong Zhao[3], Jinmei Ding[3], Xiangyu Pei[1], Fei Zhang[1], Zhengning Xu[1], Ruifang Shi[1], Ya Wei[1], Lu Zhang[3], Lingling Jin[3,*], Zhibin Wang[1,2,*]

[1] State Key Laboratory of Soil Pollution Control and Safety, Zhejiang Provincial Key Laboratory of Organic Pollution Process and Control, College of Environmental and Resource Sciences, Zhejiang University, Hangzhou 310058, China
[2] ZJU-Hangzhou Global Scientific and Technological Innovation Center, Zhejiang University, Hangzhou 311200, China
[3] Ecological and Environmental Monitoring Center of Zhejiang Province, Hangzhou 310012, China

Correspondence to: Zhibin Wang (wangzhibin@zju.edu.cn) and Lingling Jin (jinlingling@zjemc.org.cn)

Abstract. The effective density (ρ_{eff}) is closely associated with the aging process and can serve as a tracer for chemical composition. Recently, studies investigating the effect of particle size on density have been limited. In this study, size-resolved ρ_{eff} was characterized with a tandem of an aerodynamic aerosol classifier (AAC) and a scanning mobility particle sizer (SMPS) system during one month of observation in Hangzhou. The results indicate that the ρ_{eff} values of the particles exhibit a unimodal distribution, with average values ranging from 1.47 g/cm^3 to 1.63 g/cm^3, increasing as the particle diameter increases. The diurnal variation is more pronounced for small particles (d_{ae} <350 nm), which generally exhibit lower density during the day and higher density at night. The relationship between ρ_{eff} and particle diameter varies under different pollution conditions due to differences in the chemical composition of the particles. The SHapley additive explanations (SHAPs) revealed good relationships between ρ_{eff} and the bulk composition of particles with diameters smaller than 350 nm, while the relationship of larger particles was weak. Since determining the size-resolved chemical composition of particles remains challenging, a new method to investigate the size-resolved chemical composition was proposed, in which the size-resolved composition can be derived from the ρ_{eff} and fixed material density of secondary inorganic aerosols (SIAs), organic aerosols (OAs) and black carbon (BC).

1 Introduction

Atmospheric aerosols play important roles in human health, air quality, and climate change. The environmental and health impacts of aerosols are largely determined by their chemical and physical properties (Spencer et al., 2007). Density (ρ) is one of the most important physical properties of particles. Limited by techniques for measuring ρ for aspherical aerosol particles, ρ_{eff} has been commonly adopted as an alternative to aerosol density (Peng et al., 2021). It has been largely reported that ρ_{eff} is related to the particle optical properties (Zhao et al., 2019), aging process (Peng et al., 2016; Leskinen et al., 2023), and chemical composition (Spencer et al., 2007). Therefore, an understanding of size-resolved ρ_{eff} is important for accurately estimating the effects of particles on climate and health.

Currently, several systems have been developed to measure the size-resolved ρ_{eff}. The Micro Orifice Uniform Deposit Impactor (MOUDI), whose size distribution is measured simultaneously, is a commonly used off-line instrument to measure size-resolved density (Hu et al., 2012). It collects size-segregated aerosols with different size ranges and subsequently analyses their mass and chemical components, but the temporal resolution of this offline method is relatively low, and the size range is limited (0.056 – 18 μm, depending on size stages of the MOUDI used). The most commonly used method is to measure the mobility diameter and mass simultaneously, after which the ρ_{eff} of the particles can be calculated directly, including the tandem differential mobility analyzer (DMA) and mass analyzer, i.e., the aerosol particle mass analyzer (APM) and centrifugal particle mass analyzer (CPMA) (McMurry et al., 2002; Zhou et al., 2022; Xie et al., 2024). However, the particles are required to be charged before classification for DMA and APM/CPMA, which introduces multiple charge effects. Particles with higher-order charges can be selected, causing uncertainties in the ρ_{eff} calculation. Additionally, ρ_{eff} can be derived from the relationship between d_m and the (vacuum) aerodynamic diameter (d_{ae}), such as the tandem system of AAC and SMPS (Tavakoli and Olfert, 2014; Song et al., 2022b; Lu et al., 2024) and the tandem system of ultrafine aerosol time-of-flight mass spectrometry (UF-ATOFMS) and DMA, with the latter also providing size-resolved chemical composition (Spencer et al., 2007). AAC is a novel method that classifies particles on the basis of their relaxation time, which can avoid multiple charging effects (Tavakoli and Olfert, 2013). Moreover, the transmission efficiency of AAC is 2.6-5.1 times higher than that of a combined Krypton85 radioactive neutralizer and DMA (Johnson et al., 2018). Currently, the AAC-SMPS is commonly used for laboratory-generated particles, but studies on the aerodynamic size-dependent ρ_{eff} of ambient particles are still limited (Tavakoli and Olfert, 2014; Yao et al., 2020; Kazemimanesh et al., 2022; Lu et al., 2024).

The size dependence of particle ρ_{eff} has been reported in previous studies, and the variation in ρ_{eff} is associated with the chemical composition. Generally, the material densities of inorganic aerosols, such as $(NH_4)_2SO_4$ and NH_4NO_3, are higher than those of OAs. The ρ_{eff} of the particles is greater when SIA is predominant than when OA is predominant. The ρ_{eff} increases with the addition of hygroscopic substances, particularly $(NH_4)_2SO_4$ and NH_4NO_3 (Yin et al., 2015). The material density of OAs varies among different sources, but it is greater for secondary organic aerosols (SOAs) than for primary organic aerosols (POAs) (Zhou et al., 2022). The formation of secondary organic aerosols during active photochemical reactions and the aging process also leads to an increase in ρ_{eff} (Lin et al., 2018; Xie et al., 2024). The material density of BC is 1.8 g/cm^3, but ρ_{eff} can be much lower because of its fractal morphology. A decrease in ρ_{eff} was observed when primary emissions increased, which led to the accumulation of POA and BC (Lu et al., 2024; Xie et al., 2024).

However, how the chemical composition influences ρ_{eff} remains unclear because of the complexity of the species composing the particles. Currently, machine learning (ML) methods, such as simulation of ozone concentration and reproduction of aerosol number concentration, are widely used in atmospheric science research (Song et al., 2022a; Cheng et al., 2024; Zhang et al., 2024). ML can identify the complex and nonlinear relationships between input features and output predictor variables. Random forest (RF) is a commonly-used machine learning algorithm. Compared to other ML models, such as deep learning models, it maintains a commendable balance between predictive performance and interpretability (Cheng et

65 al., 2024). The SHAP proposed by Lundberg and Lee (2017) is commonly used to explain the outputs of ML models, which can be used to understand the drivers of variations in ρ_{eff}.

In this study, we present the characteristics of ambient aerosols ρ_{eff} based on one-month online measurements in Hangzhou. The diurnal variation in ρ_{eff} and the influences of the pollution level and air mass transport were discussed. ML and SHAP were applied to analyze the relationship between ρ_{eff} and the chemical composition of aerosols. The material densities of OA
70 and BC were determined from the mean ρ_{eff} and bulk chemical composition, and the size-resolved chemical composition was inferred from ρ_{eff} and compared with the bulk chemical composition.

2 Experiments

2.1 Sampling site and instrumentation

One-month continuous observations were conducted from the 9th Sept., 2023, to the 8th Oct., 2023, at the Central Air Quality
75 Assurance Monitoring Station for the 19th Asian Games in Hangzhou (CASA site). The CASA site (30.25°N, 120.24°E) is located in western Hangzhou city, which is one of the most developed cities in the Yangtze River Delta (YRD) (Fig. S1). The CASA site is near the Qiantang River, located just 100 m away. There is an elevated road 1.9 km northeast of the site and another 3.2 km southwest. The surrounding area is mainly residential and commercial, with no significant sources of pollution. The local influence at the site is primarily from residential activities and traffic emissions.
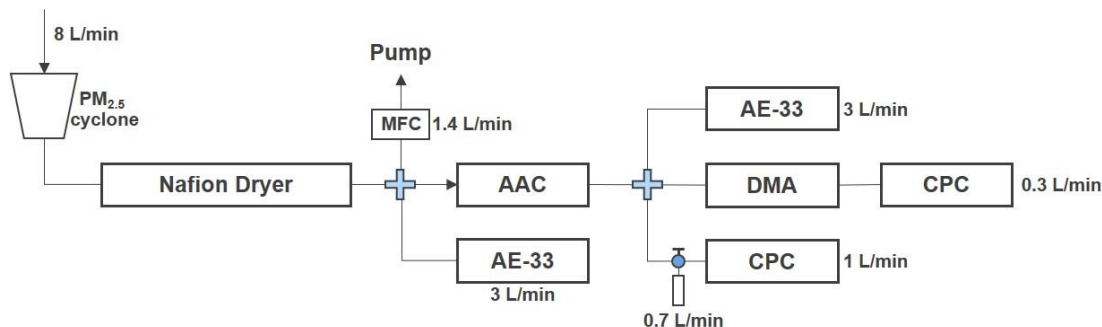
80

Figure 1: Instrumental setup used in this study. MFC: Mass flow controller.

A schematic diagram of the measurement settings is shown in Fig. 1. The particles were sampled with a PM$_{2.5}$ cyclone inlet (8 L/min) and then passed through a Nafion dryer to reduce the relative humidity (RH) to less than 30%. The sampling flow was split into three lines. One line was fed to an AAC-SMPS to determine the effective densities of particles with different
85 diameters. Another line was connected to a seven-wavelength aethalometer (Model AE-33, Magee Scientific, sample flow rate of $Q = 3$ L/min) to measure the mass concentration of black carbon (BC). The remaining flow was maintained as a bypass flow with an extra pump to ensure an accurate cutoff size. Particles with 12 logarithmically equally distributed aerodynamic sizes ranging from 200-1000 nm were selected by an AAC (Cambustion Ltd., UK, sheath flow rate $Q_{\text{sh}} = 9$ L/min and relaxation time resolution $R_{\text{t}} = 2.5$), and each size was sampled for 5 min. After the AAC classification, the aerosol flow was then split

3

into three parallel lines. One line led to a condensation particle counter (CPC, Model 3772, TSI Inc., USA) to determine the concentration of the d_{ae}-selected particles. The flow rate of the CPC was decreased to 0.3 L/min, with a bypass flow of 0.7 L/min. The second line directed the flow to an AE-33. The results of the CPC and AE-33 downstream of the AAC will be discussed in other studies. In the remaining line, the particle number size distribution (PNSD) of each d_{ae}-selected particle was acquired using an SMPS, which consisted of a soft X-ray neutralizer (Model 3088, TSI Inc., USA), a DMA (Model 3081, TSI Inc., USA., sheath flow rate Q_{sh} = 3 L/min) and a CPC (Model 3756, TSI Inc., USA., sample flow rate Q_a = 0.3 L/min). The mobility diameter range was 13.8-749.9 nm with a total scan time of 4 minutes. The modal mobility diameter of the d_{ae}-selected particles, denoted as d_m, was determined by fitting the PNSD to a log-normal distribution (Eq. S4). However, owing to the low concentrations of larger particles selected by the AAC and the inability to fit the mode ρ_{eff} from ρ_{eff} distributions scanned by the SMPS, only particles with mobility diameters smaller than 600 nm were fitted to lognormal distributions. The bulk chemical composition of nonrefractory aerosols, i.e., the mass concentrations of OA, nitrate, sulfate, ammonium and chloride, was measured via an aerosol chemical speciation monitor (ACSM; Aerodyne Research, Inc.). Combined with the BC mass concentration, the effective density ($\rho_{eff,cal}$) can be calculated with Eq. 1 (Levy et al., 2013):

$$\frac{1}{\rho_{eff,cal}} = \sum_i \frac{f_i}{\rho_i}, \tag{1}$$

where ρ_i and f_i denote the effective density and mass fraction of chemical component i, respectively. The values of effective density of BC and OA are discussed in Section 3.4.

The AAC and SMPS used in this study were calibrated with certified polystyrene latex (PSL) spheres (Thermo Fisher Scientific Inc., USA) with sizes of 152±5 nm, 203±5 nm, 303±8 nm, and 508±8 nm (Fig. S2). The d_{ae} measured by the AAC was compared with the aerodynamic diameter of the PSL ($d_{ae,PSL}$), which was calculated from the nominal diameter ($d_{m,PSL}$) and material density of the PSL (1.05 g/cm^3). The d_m determined by the SMPS was compared to the nominal diameter of the PSL. The deviations between the measured d_{ae} (d_m) and $d_{ae,PSL}$ ($d_{m,PSL}$) were 3.19% and 2.48%, respectively. The performance of the AAC-SMPS tandem system was first validated with PSL particles and the average effective density of 1.045 g/cm^3 was determined, which is consistent with the material density of PSL (1.05 g/cm^3) (Fig. S3). Then the system was validated by ammonium sulfate (AS) and ammonium nitrate (AN) particles generated with an atomizer (Model 3079A, TSI, Inc., USA). The effective densities of the size-resolved AS and AN particles are shown in Fig. S2c. The effective densities of AS particles of different sizes are within the range of 1.68–1.82 g/cm^3, which is consistent with previous studies (Yao et al., 2020; Lu et al., 2024). The measured average ρ_{eff} of AN particles was 1.80 g/cm^3, which is slightly higher than the mean ρ_{eff} of 1.69±0.17 g/cm^3 measured via DMA and a quartz crystal microbalance (QCM) (Sarangi et al., 2016).

2.2 Machine learning

The RF models were built with the "RandomForestRegressor" function provided by "scikit-learn" in a python environment (Pedregosa et al., 2011). In the RF models, the independent variables are the size-resolved effective densities of particles with different diameters. The explanatory variables are the mass fractions of the main components of PM$_{2.5}$, i.e., OA, (NH$_4$)$_2$SO$_4$,

4

NH_4NO_3, NH_4Cl and BC. The RF model was trained with a portion of the samples drawn from the whole dataset, while the remaining samples were used for model validation. To obtain an optimal RF model, the hyperparameters for the RF model were tuned via the function "GridSearchCV" from the "scikit-learn" library (Song et al., 2022a). The coefficient of determination (R^2) was used to evaluate the performance of the ML model. The best hyperparameters (n_estimators, min_samples_split, max_features, bootstrap, max-samples) of the RF model and R^2 values for particles of different sizes are listed in Table S1. The SHAP approach was implemented via the "shap" python package.

2.3 Back trajectories

The regional-scale transport patterns were investigated via back-trajectory calculations with the open-source software Meteoinfo developed by Wang (2019). The model was run 48 h backward every hour from an altitude of 5 m above the site. The NCEP Global Data Assimilation System (GDAS) model with a grid resolution of 1°×1° and a run time of 48 h each day from August to October 2023 was used in the calculations, followed by K-means clustering to investigate sources of air masses, which has been widely used in previous studies (Xu et al., 2023). All the data in this study were in Beijing time.

3. Results and discussion

3.1 Size-resolved effective densities

The average ρ_{eff} values for particles with aerodynamic diameters of 200, 235, 277, 326, 384, 452, and 531 nm were 1.47±0.09, 1.50±0.09, 1.52±0.08, 1.55±0.08, 1.58±0.08, 1.60±0.08, and 1.63±0.10 g/cm^3, respectively (Fig. 2). The distribution of ρ_{eff} was fitted to a unimodal Gaussian distribution, whereas some previous studies reported a bimodal distribution, i.e., a mode with higher peak value and larger effective density, denoted as main-density mode and another mode with lower peak value and lower effective density denoted as sub-density mode. The unimodal distribution denotes an internally mixed aerosol composition and the bimodal distribution with a second, below unity density peak indicates externally mixed BC (Qiao et al., 2018; Ma et al., 2020; Zhou et al., 2022; Xie et al., 2024). In many studies, the frequency of bimodal distribution is not comparable and largely depends on the distance between the observation points and the emission sources (Zhou et al., 2022; Wu et al., 2023; Xie et al., 2024). The occurrence of the sub-density mode is greater at sites close to the emission source. The sub-density particles predominated near the street with higher traffic emissions, whereas in the rural background, the main-dense particles dominated (Rissler et al., 2014). A lower frequency of sub-density events indicates that the particles are more likely to be in an internal mixing state. Black carbon, a major product of fossil fuel and biomass combustion, is a tracer of primary emissions (Briggs and Long, 2016). On the one hand, the bimodal distribution may not have been detected due to the absence of fresh BC. The diameter of fresh BC mainly ranges from 50-120 nm (Bond et al., 2013), which was much smaller than the selected particles in our study. On the other hand, a previous study indicated that when the ratio of the mass concentration of black carbon to $PM_{2.5}$ is less than 20%, particles with diameters between 50 and 350 nm are predominantly in an internal mixing state (Wu et al., 2023). Moreover, the smaller number of soot particles might be shadowed in the dominant

mode of the measurement (Yin et al., 2015). Unfortunately, we did not measure the chemical composition of particles of different sizes, and the bulk chemical composition revealed that the average proportion of BC to $PM_{2.5}$ was only 11% in our

155   study. Therefore, only a unimodal Gaussian fit of ρ_{eff} was identified, indicating that the particles in Hangzhou tend to internally mixed.
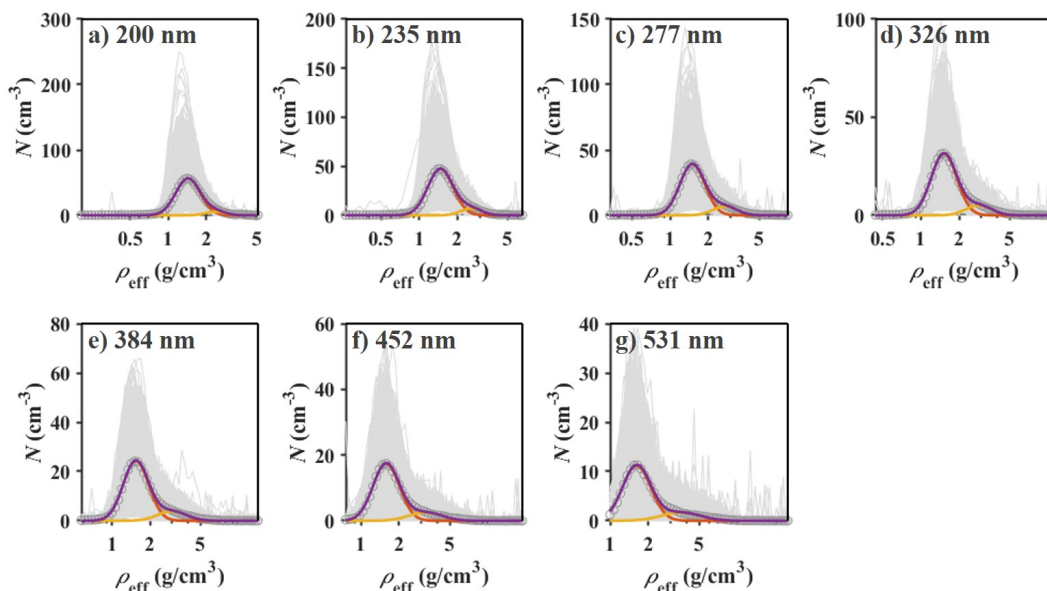

Figure 2: Averaged particle ρ_{eff} distributions at (a) 200 nm, (b) 235 nm, (c) 277 nm, (d) 326 nm, (e) 384 nm, (f) 452 nm, and (g) 531 nm. The gray lines represent the measured ρ_{eff} distributions. The red and yellow lines are the Gaussian fits of the average ρ_{eff} and
160   **the Gaussian fits of doubly charged particles, respectively. The purple line represents the sum of Gaussian fits.**

We also compared the ρ_{eff} values of the particles with those reported in other studies (Fig. 3). Notably, in this study, particles with aerodynamic diameters were selected by the AAC, but generally, the particle mobility diameter was selected in previous studies. Therefore, the mobility diameters reported in previous studies were first converted to aerodynamic diameters for comparison with the results of our study. The results revealed that the particle ρ_{eff} in most urban regions has a unimodal

165   distribution, with relatively high densities ranging from 1.2 g/cm³ to 1.8 g/cm³ (Yin et al., 2015; Xie et al., 2017; Lin et al., 2018; Lu et al., 2024). The bimodal distribution of particle ρ_{eff} was found primarily in remote areas and near highways (Rissler et al., 2014; Ma et al., 2017; Ma et al., 2020; Zhou et al., 2022; Xie et al., 2024). Specifically, in the bimodal distribution, the main-density mode corresponds to a higher ρ_{eff} and increases with increasing particle size, which is similar to that in urban areas. In contrast, the ρ_{eff} of the sub-density mode was generally less than 1 g/cm³ and decreased with increasing particle

170   diameter. The difference between urban and rural sites can be attributed to differences in the mixing state of the particles. Due to effective secondary organic aerosol formation and emissions from various sources, particles tend to mix internally in urban areas (Ching et al., 2019), leading to a unimodal distribution. Additionally, traffic emissions promote the occurrence of bimodal distributions, and it has been reported that particles are more externally mixed in street canyons and near highways (Rissler et

al., 2014; Riemer et al., 2019). In rural sites, the high frequency of bimodal distribution was determined when the observation
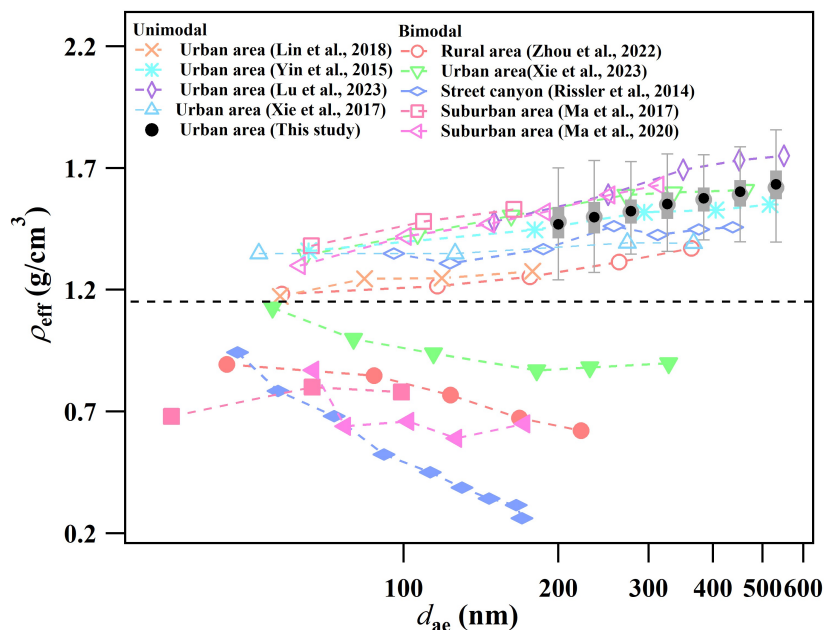175 site was influenced by local emissions (Zhou et al., 2022).

Figure 3: Size dependency of ρ_{eff} during the observations in this study. The boxes contain the 25th (Q1) and 75th (Q3) boxes. The distance between Q3 and Q1 is the interquartile range (IQR), and the whiskers extend from each quartile to the minimum or maximum. The dots inside the box represent the mean value of ρ_{eff}. The size dependency of the effective densities from previous
180 **studies is also included for comparison. The black dashed line is drawn to guide the eye.**

3.2 Diurnal variations in the effective density

Figure 4 shows the diurnal cycle of ρ_{eff} for particles with diameters of 200 nm and 531 nm, along with meteorological parameters and mass fractions of different chemical compositions of bulk particles. The diurnal variations in ρ_{eff} of the seven d_{ae}-selected particles are shown in Fig. S4. The results indicated that, in comparison with larger particles, smaller particles (d_{ae}
185 <350 nm) exhibit more pronounced diurnal variations in ρ_{eff}, typically showing lower values during the day and higher values at night (Fig. 4a). From 7:00 to 9:00, with increasing fresh black carbon (BC) and hydrocarbon-like organic aerosols (HOAs) from vehicle emissions (Fig. 4b), the ρ_{eff} of small particles decreases significantly. The volatile and gas–particle partitioning properties of $(NH_4)_2SO_4$ and NH_4Cl are dependent on the ambient T and RH (Sun et al., 2012). Although the atmospheric oxidative capacity increases later (Fig. S5), the photochemical production of HNO_3 cannot compensate for evaporative loss
190 under relatively high temperatures (Zhang et al., 2015). The mass fraction of nitrate decreased continuously from 7:00 to 13:00. Moreover, SOA formation increased significantly during this period. As a result, the fraction of high material component decreased, whereas OAs with low material density accumulated, leading to a decrease in ρ_{eff}. Although the mass fraction of secondary inorganic particles subsequently remained relatively low, ongoing atmospheric aging may cause more small

particles to have a spherical morphology (Wang et al., 2017; Wang et al., 2021). This explains why the ρ_{eff} of fine particles gradually increased between 13:00 and 17:00, even though the proportion of high-density components, such as secondary inorganic components, did not significantly increase. After 17:00, the ρ_{eff} values of the small particles did not decrease with increasing BC (Fig. S6f) and POA (Fig. S6g) emissions. Instead, it continued to rise, reaching a peak at 23:00, and then remained relatively stable. During this period, the increasing RH and decreasing temperature facilitated the redistribution of HNO_3 into the particulate phase (Sun et al., 2018; Kuang et al., 2021) and promoted the liquid-phase formation of nitrates on aerosol surfaces (Wang et al., 2020). This led to a dramatic increase in the proportion of SIA, especially for nitrates (Fig. S6d); therefore, the ρ_{eff} of the small particles did not decrease despite the decrease in the concentration of primary emitted particles such as BC and HOA.

In addition, compared to small particles, the diurnal variation in effective density of large particles is less pronounced (Fig. S4). The decreasing trend during 7:00 to 13:00 becomes less obvious, primarily because larger particles have longer residence times in the atmosphere and are less influenced by fresh emissions, resulting in a more stable chemical composition (Zhai et al., 2017; Xie et al., 2024). Overall, the effective density of large particles shows a slight increase throughout the day. This may be related to the increase in RH at night. which facilitates the formation of SIA which has been discussed before. However, compared with smaller particles, larger particles exhibit reduced surface reactions and adsorption capacity due to their lower specific surface area (Okuda, 2013). As a result, the ρ_{eff} of larger particles was less sensitive to changes in temperature and RH.
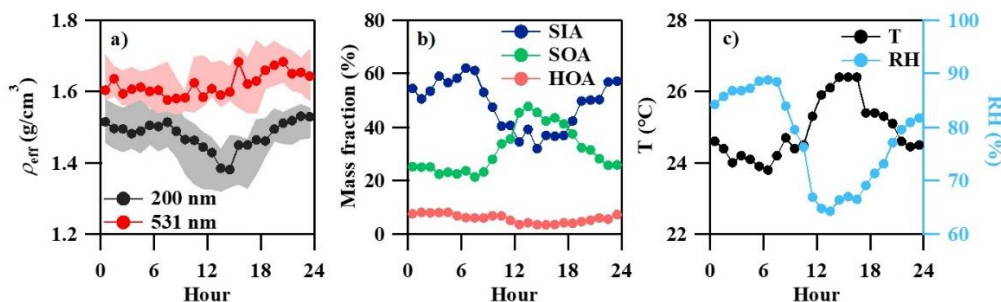

Figure 4 Diurnal variations in a) size-resolved ρ_{eff}, b) mass fractions of the main components and c) metrological parameters during the whole observation period.

3.3 Influence of different pollution levels on the particle effective density

In general, the ρ_{eff} values of particles are influenced mainly by their chemical composition and morphology, which are driven by their atmospheric oxidative capacity, RH, and temperature. Two episodes were identified to further explore the evolution of the particle ρ_{eff} (Fig. S7). Episode 1 (EP1) and episode 2 (EP2) occurred from 18:00 on the 9th to 18:00 on the 12th Sept and from 17:00 on the 23rd to 12:00 on the 30th Sept, respectively, with the remaining period defined as the clean period (CP). The PM$_{2.5}$ concentrations of EP1 and EP2 were significantly greater than that of CP (11.4 μg/m^3), with average concentrations of 27.9 and 44.7 μg/m^3, respectively. EP1 was dominated solely by organic components, which accounted for 64.1±8.0% on

average, whereas EP2 was dominated by organic and nitrate components, which accounted for 40.0±13.5% and 29.4±12.9%, respectively.

The average size-resolved effective densities and bulk chemical compositions under different pollution conditions are shown in Fig. 5. The ρ_{eff} values of all the particles increased with increasing particle size except during EP2. Interestingly, the ρ_{eff} of the particles during EP1 (1.47 to 1.61 g/cm^3) was smaller than that during CP, which is similar to the observations in the North China Plain (Zhou et al., 2022), indicating that the compositions of particles of the same size are different under different pollution levels. The proportion of OAs reached 64.1%, significantly higher than that during CP (49.3%). Previous studies reported that the effective density of organic materials was between 1.2 and 1.4 g/cm^3, which is lower than that of inorganic materials (Levy et al., 2013). Therefore, the small ρ_{eff} values of all the particles during EP1 could be attributed to the high proportion of OAs. Additionally, air mass cluster analysis indicated that the pollution during EP1 was influenced primarily by regional transport, with a shorter transportation distance than that during CP (Fig. 5d). As a result, the particles had not fully aged and remained in a relatively fractal structure, leading to a lower effective particle density during EP1.

Another interesting phenomenon is that during EP2, the ρ_{eff} of the particles did not increase with increasing particle size. For particles smaller than 400 nm, the average ρ_{eff} (1.51 to 1.55 g/cm^3) was greater than that of CP (1.40 to 1.51 g/cm^3), whereas for particles larger than 400 nm, the average ρ_{eff} (1.54 to 1.56 g/cm^3) was lower than that of CP (1.56 to 1.64 g/cm^3). We attempt to explain this phenomenon from two perspectives. First, a small particle size results in a large specific surface area, which promotes the formation of secondary inorganic components. As shown in Fig. 5b, the proportion of secondary inorganic compounds during EP2 was as high as 53.2%, which was much higher than the 37.3% observed during CP. Secondary nitrate was the most prominent component, contributing 29.2%. The diurnal variations in size-resolved particles during different periods are shown in Fig. S8. During EP2, from 13:00 to 19:00, the ρ_{eff} of small particles was significantly greater than that during CP. This difference gradually decreased over time, from a peak of 7.3% at 13:00 to 4.7% at 7:00. This suggests that nitrate formation on small particles was more pronounced during EP2. A previous study revealed that the formation of atmospheric nitrate at high temperatures was due to enhanced heterogeneous processes associated with the aerosol water concentration (Wang et al., 2020). The heterogeneous hydrolysis of N_2O_5 was the main mechanism of nitrate formation at night, which was also promoted by high RH and low temperature (Liu et al., 2020). Our observations revealed that the RH and temperature were 81.6% and 26.4°C, respectively, during EP2, which were significantly higher than those of 78.3% and 23.8°C, respectively, during CP. These results are favorable for nitrate formation on small particles during EP2. Additionally, during EP2, the air mass passing over regions such as Jiangsu and northern Zhejiang carried a high load of anthropogenic pollutants, including SO_2 (Fig. 5c). All of these factors resulted in higher precursor concentrations and enhanced the formation of secondary inorganic compounds, particularly on smaller particles. Consequently, the ρ_{eff} of the particles during EP2 remained relatively unchanged with increasing particle size.
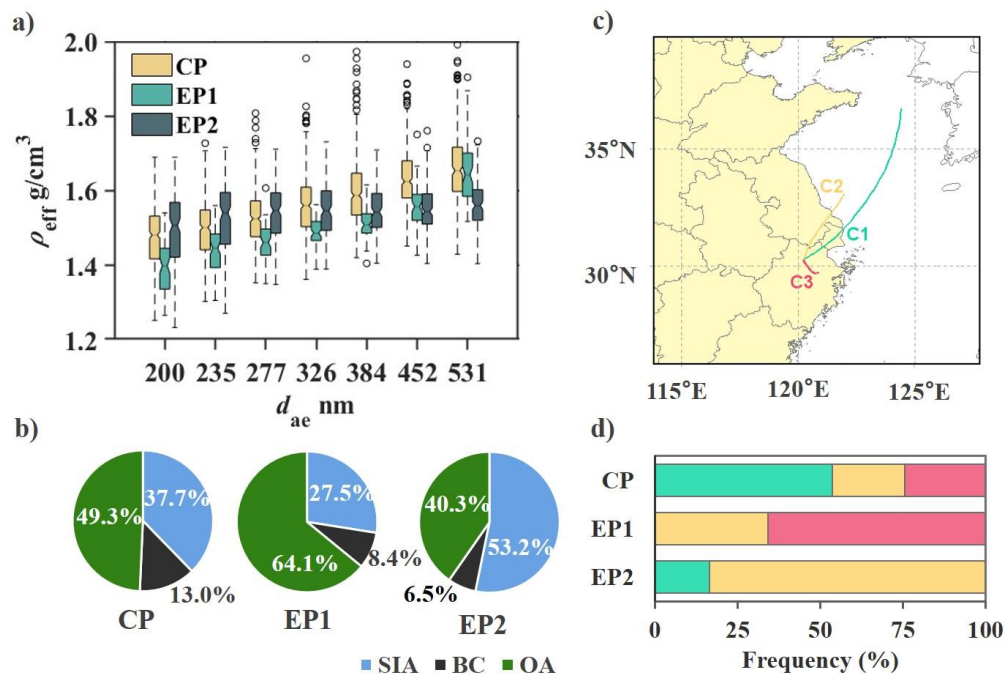
Figure 5 a) Size-resolved ρ_{eff} of particles with different diameters and b) chemical composition of PM$_{2.5}$ at different pollution levels. (c) Mean 48-h back trajectories of clusters during the measurement period. d) Proportion of different clusters at different pollution levels.

3.4 The influence of chemical composition on the particle effective density

The chemical composition of a particle is the main factor affecting its ρ_{eff}. Inorganic components, such as NH$_4$NO$_3$ and (NH$_4$)$_2$SO$_4$, have higher densities than organic compounds and BC. Therefore, variations in aerosol chemical composition can partly explain the observed trend of effective densities. Typically, the size-resolved chemical composition is measured via an aerosol mass spectrometer (Zhang et al., 2005) and single-particle mass spectrometry (Zhai et al., 2017). Due to limitations in measurement techniques, the size-resolved chemical composition of particles is not accurately measured in most studies. Here, the SHAP method was used to explore the response of different chemical components at every measured particle size on the ρ_{eff} of the particles. The cross-validation was used to evaluate the model performance, and the results suggested that the RF model performed well for particles smaller than 350 nm, with an overall R^2 score being greater than 0.55 (Table S1). In contrast, the correlation for larger particles was weaker, possibly because the chemical component variability of larger particles is smaller, resulting in inadequate modeling of these particles. For small particles, organics, NH$_4$NO$_3$, and NH$_4$Cl are the most important chemical components affecting their ρ_{eff} values (Fig. 6). Specifically, the contribution of the organic proportion was the greatest, with an average contribution of 42.9%. However, this response is negative, indicating that the ρ_{eff} of smaller particles decreases with increasing proportion of organics. NH$_4$NO$_3$ and NH$_4$Cl, which account for 32.2% and 12.7%,

10

270   respectively, were positively correlated with ρ_{eff}, suggesting that the increase in the proportion of these components mainly leads to a significant increase in the ρ_{eff} of the small particles.

    Considering the difficulty of measuring the size-resolved chemical components of particles, this study attempted to calculate the size-resolved composition according to the size-resolved ρ_{eff}. According to Eq. 1, the effective densities of the ambient OA and BC are needed. For simplicity, the particles were assumed to consist of three components, e.g., OA, SIA, and

275   BC. The value of 1.77 g/cm^3 for SIA was adopted in this study. A BC material density in the range of 0.3-2 g/cm^3 and an OA material density in the range of 1.2-1.8 g/cm^3 were used in the sensitivity test. A step length of 0.02 g/cm^3 was adopted for both the BC density and OA density. The mean ρ_{eff} is the number concentration weighted average density of particles of different sizes. The optimal values of OA and BC were determined by comparing the calculated bulk ρ_{eff} with the average ρ_{eff} for particles with diameters in the range of 200–532 nm. As a result, an OA density of 1.20 g/cm^3 and a BC density of 1.77

280   g/cm^3 were determined. The BC density of 1.77 g/cm^3 can be attributed to the coating of nitrate since nitrate contributed the most to the mass fraction of PM$_{2.5}$. The ρ_{eff} values of BC were reported to be in the range of 1.62–1.77 g/cm^3 for particles with aerodynamic diameters of 200, 350 and 500 nm in Shanghai, indicating the coating of NH$_4$NO$_3$ and/or (NH$_4$)$_2$SO$_4$ (Wang et al., 2021). The mean ρ_{eff} can be fitted well applying the results of OA and BC, with an R^2 of 0.56 (Fig. 7a).

    We apply the fitted densities of OA and BC to Eq. 1. Then, the equation is expressed as

285
$$\frac{1}{\rho_{eff}} = \frac{f_{OA}}{\rho_{OA}} + \frac{f_{BC}}{\rho_{BC}} + \frac{f_{SIA}}{\rho_{SIA}}, \qquad\qquad (2)$$

where ρ_{OA} is 1.2 g/cm^3, ρ_{BC} is 1.77 g/cm^3, and ρ_{SIA} is 1.77 g/cm^3. ρ_{eff} is the size-resolved ρ_{eff} measured by the AAC-SMPS. A series of fractions of OA, BC, and SIA were set to calculate ρ_{eff} via Eq. 2, and the fractions of OA, BC, and SIA were adjusted until the difference between the calculated and measured ρ_{eff} values was the minimum value and within an acceptable range (0.5%). Consequently, the scatter plots and time series of the size-resolved proportions of OAs during the observation were

290   determined, as shown in Fig. 7. The slope between the measured and calculated mass fractions of OAs reaches 0.65 for particles with d_{ae}<350 nm, indicating that this method can be used to deduce the chemical composition effectively. However, for larger particles (d_{ae} > 350 nm), the OA and SIA fractions can be reproduced well only during EP2 (Fig. S9), indicating that this simplified method to deduce the chemical composition is not suitable for particles with diameters larger than 350 nm unless the pollution process is dominated by OA and nitrate. We must acknowledge that this calculation would be more rigorous if

295   size-resolved chemical composition data were available. Here, we propose this method, which remains applicable if size-resolved chemical composition measurements become available in future studies. Besides, we also conducted a sensitivity analysis, which revealed that the fitting results are more sensitive to the density of BC than to that of OA (Fig. S10). For 200 nm particles, when the BC density was 1.77 g/cm³, the fitting results exhibit a higher tolerance for variations in the OA density. However, as particle size increases, this tolerance decreases. Therefore, when inferring chemical composition from effective

300   density, it is more important to accurately constrain the densities of OA and BC for larger particles.
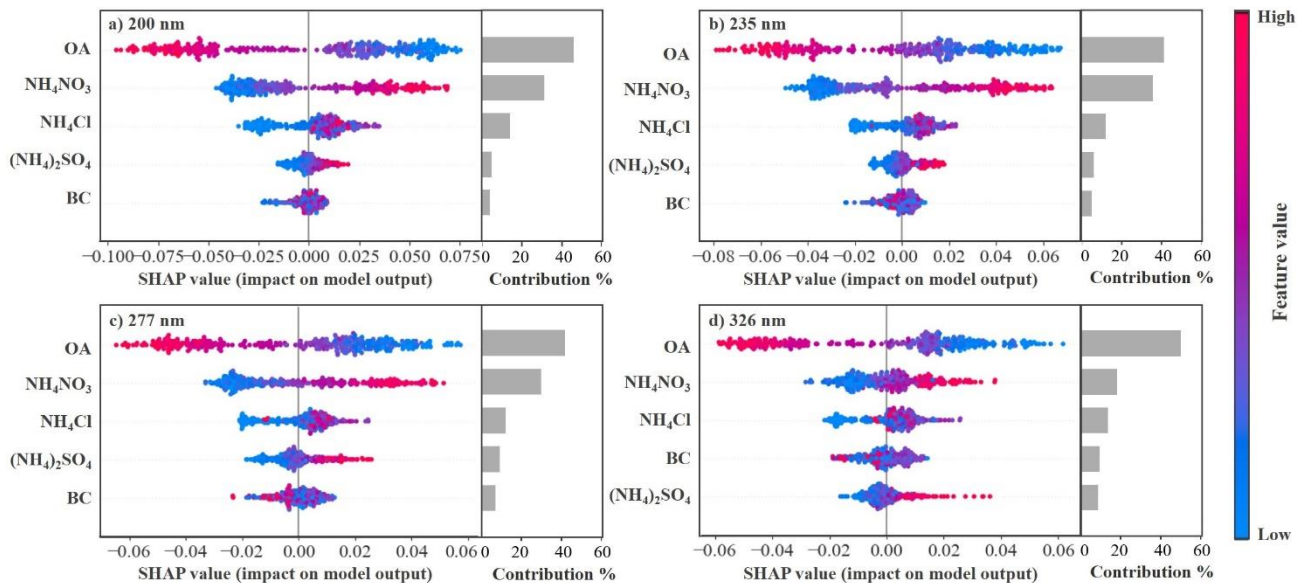
Figure 6: SHAP values of aerosol composition for particles with diameters of (a) 200 nm, (b) 235 m, (c) 277 nm and (d) 326 nm. The left bar plots attached to each panel describe the contribution of each species.
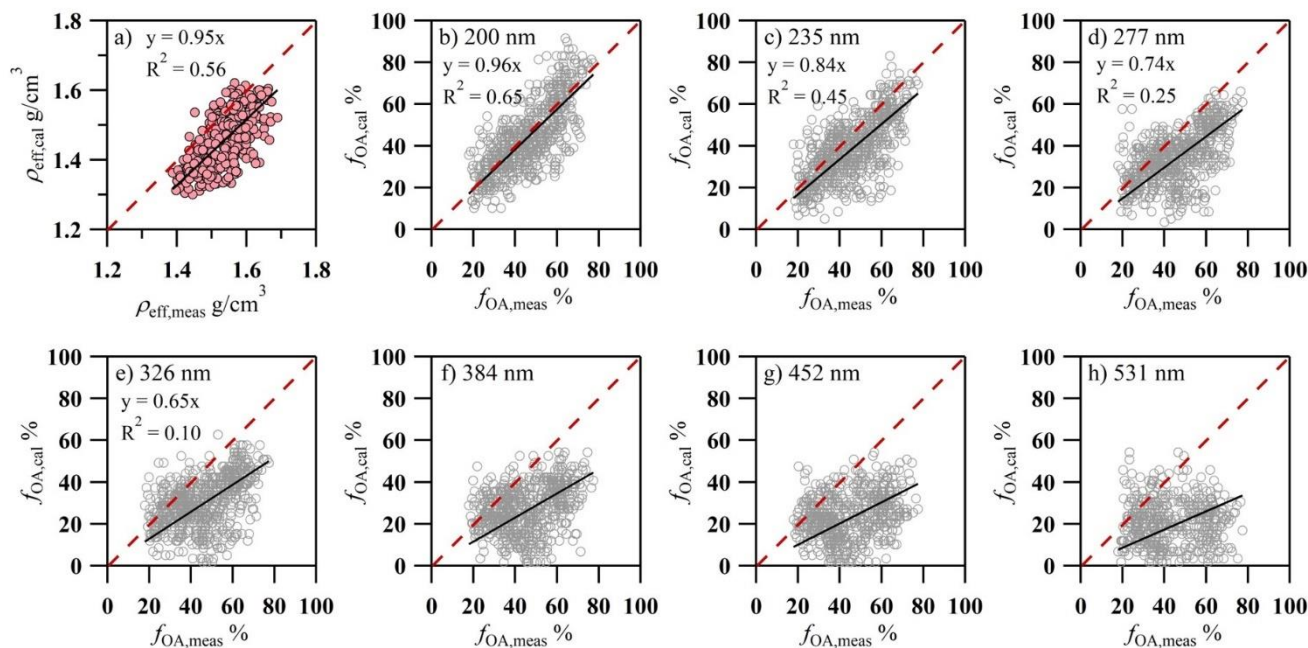

305 **Figure 7:** (a) Comparison of ρ_{eff} calculated from the ACSM aerosol composition ($\rho_{eff,cal}$) and the mean ρ_{eff} measured by the AAC-SMPS ($\rho_{eff,meas}$). Comparison of the calculated mass fraction of OAs from the measured ρ_{eff} and the measured mass fraction of OAs with an ACSM for particles with diameters of (b) 200 nm, (c) 235 nm, (d) 277 nm, (e)326 nm, (f) 384 nm, (g) 452 nm, and (h) 531 nm. The red lines denote the 1:1 line.

12

4. Conclusion

The effective density is one of the most important physical properties and is associated with the aging process and chemical composition of aerosols. In this study, the AAC-SMPS was used to characterize the size-resolved ρ_{eff} in autumn in Hangzhou. The measured ρ_{eff} distributions were fitted to unimodal log-normal distributions, and the size dependency of ρ_{eff} was determined. The ρ_{eff} varied from 1.47±0.09 to 1.63±0.10 g/cm^3 as the diameter increased from 200 nm to 531 nm. The ρ_{eff} of small particles (d_{ae}<350 nm) shows more pronounced diurnal variation due to changes in chemical composition and particle morphology, with lower values during the day and higher values at night, whereas the ρ_{eff} of larger particles shows no significant diurnal cycle. Moreover, ρ_{eff} is associated with pollution levels and air mass transport. During the clean period, ρ_{eff} is relatively high and clearly depends on size. However, during pollution episodes, the size dependence of ρ_{eff} is significantly weakened. Particularly when the pollutant components are dominated by organics and secondary nitrates, the ρ_{eff} of the particles does not increase with increasing particle size.

ML and SHAP were used to analyze the relationship between ρ_{eff} and the chemical composition of aerosols. OA, NH$_4$NO$_3$ and NH$_4$Cl have the strongest effects on ρ_{eff}. ρ_{eff} has a negative correlation with OA and positive correlations with NH$_4$NO$_3$ and NH$_4$Cl. Assuming that the particles consisted of OAs, SIAs and BCs, the material density of OAs of 1.2 g/cm^3 and that of BCs of 1.7 g/cm^3 were derived from the mean ρ_{eff} and bulk chemical composition. Using the derived material, the size-resolved chemical composition was inferred from the size-resolved ρ_{eff}. The composition can be reproduced well for small particles, but this simplified method is not suitable for particles with diameters larger than 350 nm unless the pollution process is dominated by OA and nitrate.

References

Bond, T. C., Doherty, S. J., Fahey, D. W., Forster, P. M., Berntsen, T., DeAngelo, B. J., Flanner, M. G., Ghan, S., Kärcher, B., Koch, D., Kinne, S., Kondo, Y., Quinn, P. K., Sarofim, M. C., Schultz, M. G., Schulz, M., Venkataraman, C., Zhang, H.,

345 Zhang, S., Bellouin, N., Guttikunda, S. K., Hopke, P. K., Jacobson, M. Z., Kaiser, J. W., Klimont, Z., Lohmann, U., Schwarz, J. P., Shindell, D., Storelvmo, T., Warren, S. G., and Zender, C. S.: Bounding the role of black carbon in the climate system: A scientific assessment, J. Geophys. Res.: Atmos., 118, 5380-5552, 10.1002/jgrd.50171, 2013.

Briggs, N. L., and Long, C. M.: Critical review of black carbon and elemental carbon source apportionment in Europe and the United States, Atmos. Environ., 144, 409-427, https://doi.org/10.1016/j.atmosenv.2016.09.002, 2016.

350 Cheng, Y., Peng, Y., Cao, L.-M., Huang, X.-F., and He, L.-Y.: Identifying the geospatial relationship of surface ozone pollution in China: Implications for key pollution control regions, Sci. Total Environ., 930, 172763, https://doi.org/10.1016/j.scitotenv.2024.172763, 2024.

Cheng, Y., Peng, Y., Cao, L.-M., Huang, X.-F., and He, L.-Y.: Identifying the geospatial relationship of surface ozone pollution in China: Implications for key pollution control regions, Sci. Total Environ., 930, 172763,

355 https://doi.org/10.1016/j.scitotenv.2024.172763, 2024.

Ching, J., Adachi, K., Zaizen, Y., Igarashi, Y., and Kajino, M.: Aerosol mixing state revealed by transmission electron microscopy pertaining to cloud formation and human airway deposition, npj Climate and Atmospheric Science, 2, 22, https://doi.org/10.1038/s41612-019-0081-9, 2019.

Hu, M., Peng, J., Sun, K., Yue, D., Guo, S., Wiedensohler, A., and Wu, Z.: Estimation of Size-Resolved Ambient Particle

360 Density Based on the Measurement of Aerosol Number, Mass, and Chemical Size Distributions in the Winter in Beijing, Environ. Sci. Technol., 46, 9941-9947, https://doi.org/10.1021/es204073t, 2012.

Johnson, T. J., Irwin, M., Symonds, J. P. R., Olfert, J. S., and Boies, A. M.: Measuring aerosol size distributions with the aerodynamic aerosol classifier, Aerosol Sci. Technol., 52, 655-665, https://doi.org/10.1080/02786826.2018.1440063, 2018.

Kazemimanesh, M., Rahman, M. M., Duca, D., Johnson, T. J., Addad, A., Giannopoulos, G., Focsa, C., and Boies, A. M.: A

365 comparative study on effective density, shape factor, and volatile mixing of non-spherical particles using tandem aerodynamic diameter, mobility diameter, and mass measurements, J. Aerosol Sci., 161, 105930, https://doi.org/10.1016/j.jaerosci.2021.105930, 2022.

Kuang, Y., Huang, S., Xue, B., Luo, B., Song, Q., Chen, W., Hu, W., Li, W., Zhao, P., Cai, M., Peng, Y., Qi, J., Li, T., Wang, S., Chen, D., Yue, D., Yuan, B., and Shao, M.: Contrasting effects of secondary organic aerosol formations on organic aerosol

370 hygroscopicity, Atmos. Chem. Phys., 21, 10375-10391, https://doi.org/10.5194/acp-21-10375-2021, 2021.

Leskinen, J., Hartikainen, A., Väätäinen, S., Ihalainen, M., Virkkula, A., Mesceriakovas, A., Tiitta, P., Miettinen, M., Lamberg, H., Czech, H., Yli-Pirilä, P., Tissari, J., Jakobi, G., Zimmermann, R., and Sippula, O.: Photochemical Aging Induces Changes in the Effective Densities, Morphologies, and Optical Properties of Combustion Aerosol Particles, Environ. Sci. Technol., 57, 5137-5148, https://doi.org/10.1021/acs.est.2c04151, 2023.

375 Levy, M. E., Zhang, R., Khalizov, A. F., Zheng, J., Collins, D. R., Glen, C. R., Wang, Y., Yu, X.-Y., Luke, W., Jayne, J. T., and Olaguer, E.: Measurements of submicron aerosols in Houston, Texas during the 2009 SHARP field campaign, J. Geophys. Res.-Atmos., 118, 10,518-510,534, https://doi.org/10.1002/jgrd.50785, 2013.

Lin, Y., Bahreini, R., Zimmerman, S., Fofie, E. A., Asa-Awuku, A., Park, K., Lee, S.-B., Bae, G.-N., and Jung, H. S.: Investigation of ambient aerosol effective density with and without using a catalytic stripper, Atmos. Environ., 187, 84-92,

380 https://doi.org/10.1016/j.atmosenv.2018.05.063, 2018.

Liu, L., Bei, N., Hu, B., Wu, J., Liu, S., Li, X., Wang, R., Liu, Z., Shen, Z., and Li, G.: Wintertime nitrate formation pathways in the north China plain: Importance of N2O5 heterogeneous hydrolysis, Environ. Pollut., 266, 115287, https://doi.org/10.1016/j.envpol.2020.115287, 2020.

Lu, J., Shen, X., Ma, Q., Yu, A., Hu, X., Zhang, Y., Liu, Q., Liu, S., Che, H., Zhang, X., and Sun, J.: Size-resolved effective

385 density of ambient aerosols measured by an AAC–SMPS tandem system in Beijing, Atmos. Environ., 318, 120226, https://doi.org/10.1016/j.atmosenv.2023.120226, 2024.

Ma, Y., Li, S., Zheng, J., Khalizov, A., Wang, X., Wang, Z., and Zhou, Y.: Size-resolved measurements of mixing state and cloud-nucleating ability of aerosols in Nanjing, China, J. Geophys. Res.-Atmos., 122, 9430-9450, https://doi.org/10.1002/2017jd026583, 2017.

390 Ma, Y., Huang, C., Jabbour, H., Zheng, Z., Wang, Y., Jiang, Y., Zhu, W., Ge, X., Collier, S., and Zheng, J.: Mixing state and light absorption enhancement of black carbon aerosols in summertime Nanjing, China, Atmos. Environ., 222, 117141, https://doi.org/10.1016/j.atmosenv.2019.117141, 2020.

McMurry, P. H., Wang, X., Park, K., and Ehara, K.: The Relationship between Mass and Mobility for Atmospheric Particles: A New Technique for Measuring Particle Density, Aerosol Sci. Technol., 36, 227-238,
395 https://doi.org/10.1080/027868202753504083, 2002.

Okuda, T.: Measurement of the specific surface area and particle size distribution of atmospheric aerosol reference materials, Atmos. Environ., 75, 1-5, https://doi.org/10.1016/j.atmosenv.2013.04.033, 2013.

Pedregosa, F., Varoquaux, G., Gramfort, A., Michel, V., Thirion, B., Grisel, O., Blondel, M., Louppe, G., Prettenhofer, P., Weiss, R., Weiss, R. J., Vanderplas, J., Passos, A., Cournapeau, D., Brucher, M., Perrot, M., and Duchesnay, E.: Scikit-learn:
400 Machine Learning in Python, J. Mach. Learn. Res. 12, 2825-2830, https://dl.acm.org/doi/10.5555/1953048.2078195, 2011.

Peng, J., Hu, M., Guo, S., Du, Z., Zheng, J., Shang, D., Levy Zamora, M., Zeng, L., Shao, M., Wu, Y. S., Zheng, J., Wang, Y., Glen, C. R., Collins, D. R., Molina, M. J., and Zhang, R.: Markedly enhanced absorption and direct radiative forcing of black carbon under polluted urban environments, Proc Natl Acad Sci USA, 113, 4266-4271, https://doi.org/10.1073/pnas.1602310113, 2016.

405 Peng, L., Li, Z., Zhang, G., Bi, X., Hu, W., Tang, M., Wang, X., Peng, P., and Sheng, G.: A review of measurement techniques for aerosol effective density, Sci Total Environ, 778, 146248, https://doi.org/10.1016/j.scitotenv.2021.146248, 2021.

Qiao, K., Wu, Z., Pei, X., Liu, Q., Shang, D., Zheng, J., Du, Z., Zhu, W., Wu, Y., Lou, S., Guo, S., Chan, C. K., Pathak, R. K., Hallquist, M., and Hu, M.: Size-resolved effective density of submicron particles during summertime in the rural atmosphere of Beijing, China, J. Environ. Sci., 73, 69-77, https://doi.org/10.1016/j.jes.2018.01.012, 2018.

410 Riemer, N., Ault, A. P., West, M., Craig, R. L., and Curtis, J. H.: Aerosol Mixing State: Measurements, Modeling, and Impacts, Rev. Geophys., 57, 187-249, https://doi.org/10.1029/2018RG000615, 2019.

Rissler, J., Nordin, E. Z., Eriksson, A. C., Nilsson, P. T., Frosch, M., Sporre, M. K., Wierzbicka, A., Svenningsson, B., Londahl, J., Messing, M. E., Sjogren, S., Hemmingsen, J. G., Loft, S., Pagels, J. H., and Swietlicki, E.: Effective density and mixing state of aerosol particles in a near-traffic urban environment, Environ Sci Technol, 48, 6300-6308,
415 https://doi.org/10.1021/es5000353, 2014.

Sarangi, B., Aggarwal, S. G., Sinha, D., and Gupta, P. K.: Aerosol effective density measurement using scanning mobility particle sizer and quartz crystal microbalance with the estimation of involved uncertainty, Atmos. Meas. Tech., 9, 859-875, https://doi.org/10.5194/amt-9-859-2016, 2016.

Song, C., Becagli, S., Beddows, D. C. S., Brean, J., Browse, J., Dai, Q., Dall'Osto, M., Ferracci, V., Harrison, R. M., Harris,
420 N., Li, W., Jones, A. E., Kirchgäßner, A., Kramawijaya, A. G., Kurganskiy, A., Lupi, A., Mazzola, M., Severi, M., Traversi, R., and Shi, Z.: Understanding Sources and Drivers of Size-Resolved Aerosol in the High Arctic Islands of Svalbard Using a Receptor Model Coupled with Machine Learning, Environ. Sci. Technol., 56, 11189-11198, https://doi.org/10.1021/acs.est.1c07796, 2022a.

Song, Y., Pei, X., Liu, H., Zhou, J., and Wang, Z.: Characterization of tandem aerosol classifiers for selecting particles:
425 implication for eliminating the multiple charging effect, Atmos. Meas. Tech., 15, 3513-3526, https://doi.org/10.5194/amt-15-3513-2022, 2022b.

Song, Y., Wei, J., Zhao, W., Ding, J., Pei, X., Zhang, F., Xu, Z., Shi, R., Wei, Y., Zhang, L., Jin, L., and Wang, Z.:Data of measurement report: size-resolved particle effective density measured by the AAC-SMPS and implications for chemical composition, Zenodo [data set], https://doi.org/10.5281/zenodo.13981448, 2024
430 Spencer, M. T., Shields, L. G., and Prather, K. A.: Simultaneous Measurement of the Effective Density and Chemical Composition of Ambient Aerosol Particles, Environ. Sci. Technol., 41, 1303-1309, https://doi.org/10.1021/es061425+, 2007.

Sun, P., Nie, W., Chi, X., Xie, Y., Huang, X., Xu, Z., Qi, X., Xu, Z., Wang, L., Wang, T., Zhang, Q., and Ding, A.: Two years of online measurement of fine particulate nitrate in the western Yangtze River Delta: influences of thermodynamics and N_2O_5 hydrolysis, Atmos. Chem. Phys., 18, 17177-17190,
435 https://doi.org/10.5194/acp-18-17177-2018, 2018.

Sun, Y., Wang, Z., Dong, H., Yang, T., Li, J., Pan, X., Chen, P., and Jayne, J. T.: Characterization of summer organic and inorganic aerosols in Beijing, China with an Aerosol Chemical Speciation Monitor, Atmos. Environ., 51, 250-259, https://doi.org/10.1016/j.atmosenv.2012.01.013, 2012.

Tavakoli, F., and Olfert, J. S.: An Instrument for the Classification of Aerosols by Particle Relaxation Time: Theoretical Models of the Aerodynamic Aerosol Classifier, Aerosol Sci. Technol., 47, 916-926, https://doi.org/10.1080/02786826.2013.802761, 2013.

Tavakoli, F., and Olfert, J. S.: Determination of particle mass, effective density, mass–mobility exponent, and dynamic shape factor using an aerodynamic aerosol classifier and a differential mobility analyzer in tandem, J. Aerosol Sci., 75, 35-42, https://doi.org/10.1016/j.jaerosci.2014.04.010, 2014.

Wang, S., Zhou, K., Lu, X., Chen, H., Yang, F., Li, Q., Yang, X., and Wang, X.: Measurement of Density and Shape for Single Black Carbon Aerosols in a Heavily Polluted Urban Area, Aerosol Air Quality Res., 21, 210162, https://doi.org/10.4209/aaqr.210162, 2021.

Wang, Y., Liu, F., He, C., Bi, L., Cheng, T., Wang, Z., Zhang, H., Zhang, X., Shi, Z., and Li, W.: Fractal Dimensions and Mixing Structures of Soot Particles during Atmospheric Processing, Environ. Sci. Technol. Lett., 4, 487-493, https://doi.org/10.1021/acs.estlett.7b00418, 2017.

Wang, Y., Chen, Y., Wu, Z., Shang, D., Bian, Y., Du, Z., Schmitt, S. H., Su, R., Gkatzelis, G. I., Schlag, P., Hohaus, T., Voliotis, A., Lu, K., Zeng, L., Zhao, C., Alfarra, M. R., McFiggans, G., Wiedensohler, A., Kiendler-Scharr, A., Zhang, Y., and Hu, M.: Mutual promotion between aerosol particle liquid water and particulate nitrate enhancement leads to severe nitrate-dominated particulate matter pollution and low visibility, Atmos. Chem. Phys., 20, 2161-2175, https://doi.org/10.5194/acp-20-2161-2020, 2020.

Wang, Y. Q.: An Open Source Software Suite for Multi-Dimensional Meteorological Data Computation and Visualisation, J. Open Res. Software, https://doi.org/10.5334/jors.267, 2019.

Wu, C.-A., Chen, Y.-T., Young, L.-H., Chang, P.-K., Chou, L.-T., Chen, A. Y., and Hsiao, T.-C.: Ultrafine particles in urban settings: A combined study of volatility and effective density revealed by VT-DMA-APM, Atmos. Environ., 312, 120054, https://doi.org/10.1016/j.atmosenv.2023.120054, 2023.

Xie, T., Cao, L., Zheng, J., Xuan, P., and Huang, X.: Characterization of size-resolved effective density of atmospheric particles in an urban atmosphere in Southern China, Journal of Environmental Sciences, 141, 194-204, https://doi.org/10.1016/j.jes.2023.09.021, 2024.

Xie, Y., Ye, X., Ma, Z., Tao, Y., Wang, R., Zhang, C., Yang, X., Chen, J., and Chen, H.: Insight into winter haze formation mechanisms based on aerosol hygroscopicity and effective density measurements, Atmos. Chem. Phys., 17, 7277-7290, https://doi.org/10.5194/acp-17-7277-2017, 2017.

Xu, Z., Zou, Q., Jin, L., Shen, Y., Shen, J., Xu, B., Qu, F., Zhang, F., Xu, J., Pei, X., Xie, G., Kuang, B., Huang, X., Tian, X., and Wang, Z.: Characteristics and sources of ambient Volatile Organic Compounds (VOCs) at a regional background site, YRD region, China: Significant influence of solvent evaporation during hot months, Sci. Total Environ., 857, 159674, https://doi.org/10.1016/j.scitotenv.2022.159674, 2023.

Yao, Q., Asa-Awuku, A., Zangmeister, C. D., and Radney, J. G.: Comparison of three essential sub-micrometer aerosol measurements: Mass, size and shape, Aerosol Sci. Technol., 54, 1197-1209, https://doi.org/10.1080/02786826.2020.1763248, 2020.

Yin, Z., Ye, X., Jiang, S., Tao, Y., Shi, Y., Yang, X., and Chen, J.: Size-resolved effective density of urban aerosols in Shanghai, Atmos. Environ., 100, 133-140, https://doi.org/10.1016/j.atmosenv.2014.10.055, 2015.

Zhai, J., Lu, X., Li, L., Zhang, Q., Zhang, C., Chen, H., Yang, X., and Chen, J.: Size-resolved chemical composition, effective density, and optical properties of biomass burning particles, Atmos. Chem. Phys., 17, 7481-7493, https://doi.org/10.5194/acp-17-7481-2017, 2017.

Zhang, C., Xie, Y., Shao, M., and Wang, Q. g.: Application of machine learning to analyze ozone sensitivity to influencing factors: A case study in Nanjing, China, Sci. Total Environ., 929, 172544, https://doi.org/10.1016/j.scitotenv.2024.172544, 2024.

Zhang, J. K., Sun, Y., Liu, Z. R., Ji, D. S., Hu, B., Liu, Q., and Wang, Y. S.: Characterization of submicron aerosols during a month of serious pollution in Beijing, 2013, Atmos. Chem. and Phys., 14, 2887-2903, https://doi.org/10.5194/acp-14-2887-2014, 2014.

Zhang, Q., Canagaratna, M. R., Jayne, J. T., Worsnop, D. R., and Jimenez, J.-L.: Time- and size-resolved chemical composition of submicron particles in Pittsburgh: Implications for aerosol sources and processes, J. Geophys. Res.: Atmospheres, 110, https://doi.org/10.1029/2004JD004649, 2005.

Zhang, Y. J., Tang, L. L., Wang, Z., Yu, H. X., Sun, Y. L., Liu, D., Qin, W., Canonaco, F., Prévôt, A. S. H., Zhang, H. L., and Zhou, H. C.: Insights into characteristics, sources, and evolution of submicron aerosols during harvest seasons in the Yangtze
490 River delta region, China, Atmos. Chem. Phys., 15, 1331-1349, https://doi.org/10.5194/acp-15-1331-2015, 2015.

Zhao, G., Tan, T., Zhao, W., Guo, S., Tian, P., and Zhao, C.: A new parameterization scheme for the real part of the ambient urban aerosol refractive index, Atmos. Chem. Phys., 19, 12875-12885, https://doi.org/10.5194/acp-19-12875-2019, 2019.

Zhou, Y., Ma, N., Wang, Q., Wang, Z., Chen, C., Tao, J., Hong, J., Peng, L., He, Y., Xie, L., Zhu, S., Zhang, Y., Li, G., Xu, W., Cheng, P., Kuhn, U., Zhou, G., Fu, P., Zhang, Q., Su, H., and Cheng, Y.: Bimodal distribution of size-resolved particle
495 effective density: results from a short campaign in a rural environment over the North China Plain, Atmos. Chem. Phys., 22, 2029-2047, https://doi.org/10.5194/acp-22-2029-2022, 2022.